Journal Article

An ultra-light, low-cost reflecting/absorbing dual-mode Metasurface

Zhai, M., Zhang, T., Pei, R., He, H., Zhang, L., Leach, M., Lim, E.G., Wang, Z., Wang, J., Hua, Q., Akinsolu, M., Liu, B., Y, W.-Y., and Huang, Y.

Materials & Design 257 (2025) 114470

Contents lists available at ScienceDirect

Materials & Design

journal homepage: www.elsevier.com/locate/matdes

An ultra-light, low-cost reflecting/absorbing dual-mode metasurface

Menglin Zhai [a,b], Tian Zhang [a,b], Rui Pei [a,b,c,*], Huiwu He [a,b], Lei Zhang [a,b], Mark Leach [c], Eng Gee Lim [c], Zhao Wang [c], Jingchen Wang [c], Qiang Hua [d], Mobayode Akinsolu [e], Bo Liu [f], Wen-Yan Yin [g], Yi Huang [h]

[a] College of Information Science and Technology, Donghua University, Shanghai 201620, China
[b] Engineering Research Center of Digitalized Textile and Fashion Technology, Ministry of Education, Shanghai 201620, China
[c] School of Advanced Technology, Xi'an Jiaotong Liverpool University, Suzhou 215123, China
[d] Department of Engineering and Technology, School of Computing and Engineering, University of Huddersfield HD1 3DH Huddersfield, UK
[e] Faculty of Arts, Science and Technology, Wrexham University, LL11 2AW Wrexham, UK
[f] James Watt School of Engineering, University of Glasgow G12 8LU Glasgow, UK
[g] Innovative Institute of Electromagnetic Information and Electronic Integration, Zhejiang University, Hangzhou 310027, China
[h] Department of Electrical Engineering and Electronics, University of Liverpool, Liverpool L69 3BX, UK

ARTICLE INFO

Keywords:
Textile metasurface
Reconfigurable
Reflection
Relatively wideband absorption

ABSTRACT

This paper presents an ultra-light, low-cost reconfigurable metasurface functioning as both reflector and absorber, with mode switching via a lossy electromagnetic bandgap (EBG) layer. In reflection mode, the reflecting EBG (REBG) structure exhibits in-phase reflection characteristics at 2.48 and 5.84 GHz, with its dual-band operation achieved through a square patch configuration. In absorption mode, the integration of a lossy EBG layer atop the REBG enables relatively wideband absorption, while preserving insensitivity to polarization and exhibiting stability against varying incident angles. The absorption band fully encompasses the reflection band by employing an artificial intelligence (AI)-driven antenna optimization technique, specifically, the self-adaptive Bayesian neural network surrogate model-assisted differential evolution for antenna optimization (SB-SADEA) method. With a peak absorption rate reaching 99 %, the developed prototype sustains over 90 % absorption efficiency throughout the 2.2–7.28 GHz band. Additionally, this structure can isolate thermal infrared radiation, achieving both electromagnetic and infrared camouflage capabilities, with an infrared emissivity as low as 0.06. Two co-fabricated textile monopole antennas were experimentally characterized with the REBG to validate reflection behavior. The metasurface boosts realized gain by 5 dB at 2.48 GHz and 5.84 GHz. Consistent agreement between simulations and measurements proves the dual-mode metasurface's efficacy.

1. Introduction

Metasurfaces constructed from the periodic arrangements of metals and dielectric materials have diversified applications beyond communication and radar technology. Their utility spans imaging, stealth technology [1], metamaterial absorbers (MA) [2–6], gain-enhancement [7], and numerous other fields. This extensive applicability stems from their exceptional traits (like negative permittivity and negative permeability), largely absent in natural materials. These distinctive properties empower metasurfaces to control the direction, magnitude, and phase of electromagnetic (EM) waves. Achieving this control involves adjustments in their constituent unit cells' shape, size, and arrangement. Consequently, metasurfaces present a broad range of potential applications, harnessing their unique characteristics to manipulate EMs effectively.

Metasurfaces as reflectors in antenna structures can be used to enhance the gain of antennas [15,16]. Their arrangement of unit cells enables the focusing of EM waves toward targeted directions. Utilizing wave interference principles, the phase control method induces spatial coherence in reflected waves, dramatically boosting energy flux density in designated directions. Theoretical modeling demonstrates that carefully designed periodic metasurface structures can achieve virtually complete electromagnetic energy capture at preselected frequencies. Surface-type metamaterials (that is, metafilms or metasurfaces) offer greater design flexibility in manipulating EM properties for microwave absorption compared to conventional materials like MXene [17,18], gels

* Corresponding author at: School of Advanced Technology, Xi'an Jiaotong Liverpool University, Suzhou 215123, China.
E-mail address: rui.pei02@xjtlu.edu.cn (R. Pei).

https://doi.org/10.1016/j.matdes.2025.114470
Received 28 May 2025; Received in revised form 20 July 2025; Accepted 25 July 2025
Available online 25 July 2025

Table 1
Performance comparison with state-of-the-art designs.

Ref.	Frequency (GHz)	Thickness (mm)	ε	Material	PI	IAS	Flexibility	Reconfigurability	Infrared camouflage	CMPUV (g/cm^3)
[6]	3.6–24.6	12.5 (0.4λ)	4.4	FR4, lumped resistors, copper.	Yes	40°	No	No	/	0.1750
[8]	7–12.7	3.5 (0.12λ)	4.4	FR4, gold, copper, and resistive sheets	/	40°	No	No	Yes	1.8411
[9]	10.52–20.04	5.9 (0.3λ)	80	ITO, PET, polydimethylsiloxane, and water.	Yes	30°	Yes	Yes	Yes	1.1400
[10]	1.98–18.6	9.5 (0.33λ)	3	ITO, PET.	Yes	45°	Yes	No	Yes	0.0504
[11]	8.43–10.38	1.06 (0.03λ)	3	Paper, silver conductive ink.	Yes	45°	Yes	No	/	0.7653
[12]	8–18	3 (0.13λ)	2.9	Graphene and silicone.	Yes	30°	Yes	No	/	1.1204
[13]	10.5–11.1	1.2 (0.043λ)	1.8	Ordinary textile, silver conductive ink, and copper tape.	/	/	Yes	No	/	1.5510
[14]	8.9–15.2/ 11.2–24.1	2.6 (0.104λ/ 0.153λ)	2	Scuba knitting fabric, and metalized fabric.	/	30°	Yes	No	/	0.4551
This work	2.2–7.28	15 (0.23λ)	1.2	Felt, foam, carbon-coated film, and conductive textile.	Yes	40°	Yes	Yes	Yes	0.0550

*Working center frequency wavelength (λ), polarization insensitivity (PI), incident angle stability (IAS), dielectric permittivity (ε), calculated mass per unit volume (CMPUV).

[19], FeSiAl [20], and graphene [21]. This advantage stems from metasurfaces' ability to tailor material characteristics and structural dimensions to suit specific practical needs, allowing for precise control and customization of EM wave interactions. On the other hand, to broaden the application of electromagnetic absorbers, research on ultra-light electromagnetic wave absorbers is of significant scientific importance, especially with the rising requirement for lightweight and high-performance materials in modern communication, radar, and stealth technologies [22–24]. Additionally, traditional structures for infrared isolation often use designs involving indium tin oxide (ITO) films fabricated on ultra-thin polyethylene terephthalate (PET) substrates, or employ ITO glass coated with precious metals [8–10], which are heavy and costly. In contrast, this paper uses more affordable and lightweight materials to achieve infrared isolation and microwave absorption. The reflector designed in this paper is based on the traditional concentric square patch [25], and a comparison of several MA designs is presented in Table 1.

The concept of MA was first experimentally demonstrated by Landy et al. (2008) through their pioneering work on perfectly matched resonant structures [26], and the peak absorptivity can reach up to 99 % at 11.5 GHz, but it had a narrow absorption band and was polarization-sensitive, limiting its application. Ever since, various multi-band [3,27], wide-band [28], polarization-insensitive [6,28], and angularly stable MAs have been reported in the literature. The literature documents three established methodologies to achieve broadband performance in MA designs: The first approach is to load lumped components into absorbers and combine the resonant absorption of the material with the ohmic loss of the lumped element to achieve broadband absorption [29]. The second approach is to design a multilayer structure [27,30], and the third strategy employs a monolayer absorber architecture incorporating multiple resonators with progressively scaled dimensions to achieve broadband performance. [31,32]. In this approach, a lossy EBG layer is loaded to fuse dual bands to achieve relatively broadband absorption.

Many surface-type metamaterial (metasurface) designs rely on metallic patterns on inflexible printed circuit boards (PCB) to support the fabrication process [33], highlighting the structural geometry of EBGs rather than emphasizing the properties of the materials used. However, this approach has limited design flexibility. There is a growing demand for flexible metamaterials as they can seamlessly integrate into wearable devices without compromising electromagnetic performance. Consequently, MAs have emerged on flexible substrates like felt [34], cotton [4,35], and polydimethylsiloxane (PDMS) [36]. Several studies have investigated the fabrication of conductive patterns on flexible substrates through techniques such as conductive ink printing [11–13], graphene [12], conductive fibers [37], laser etching [5,38], cutting processes [34], and yarn embroidery [4,35]. Researchers are also investigating the enhancement of metasurfaces' functionalities by aiming for reconfigurability. Conventional reconfigurable metasurfaces typically integrate active elements, including positive-intrinsic negative (PIN) diodes [39], varactors, microelectromechanical systems (MEMS) [40], and liquid metal [41]. Recent progress in fluidic reconfigurable metasurfaces has revealed two distinct strategies: (i) ultra-wideband absorption through 3D-printed water-filled truncated cones achieving 154.5 % relative bandwidth (6.5–50.7 GHz) with thermal stability [42], and (ii) bi-functional switching between absorption (>90 % in 16.5–24 GHz) and cross-polarization conversion (4.38–11.9 GHz) via water injection control [43]. While these aqueous approaches demonstrate exceptional reconfigurability, their rigid substrates and liquid containment requirements render them incompatible with flexible textile applications. The porous characteristics of fabric substrates introduce unique challenges for metasurface implementation, including incompatibility with standard surface-mount technologies and heightened sensitivity to mechanical stress, issues exacerbated by fluidic systems' need for hermetic sealing. Hence, an optimization procedure is often required to automatically tune the geometrical parameters of textile-based metamaterials to meet their desired specifications [44], as demonstrated in our work.

Our group previously introduced the concept of applying a resistive net on top of a reflective textile EBG, as reported in [45]. The initial design, tailored for a single frequency, demonstrated through equivalent circuit modeling and current analysis that accurate impedance matching could achieve high levels of microwave absorption. Building on this foundation, this study proposes a novel multi-band structure that utilizes two distinct types of resistive materials to achieve broadband absorption. This advancement significantly enhances the design's practicality for real-world applications. Additionally, the proposed design incorporates an innovative textile-foam combination, which not only supports wideband absorption but also enables effective infrared camouflage functionality and has an additional ultra-light advantage. The optimum topological profile that ensures that the proposed reconfigurable textile metasurface exhibits absorption and reflection over absorption and reflection bands that overlap has been generated using artificial intelligence (AI). For antenna optimization, the SB-SADEA algorithm combines differential evolution (DE) with a self-adaptive Bayesian neural network surrogate model [46]. SB-SADEA, the most recent development in the SADEA algorithm series, enhances global optimization for antenna design by leveraging machine learning. It outperforms traditional methods such as particle swarm optimization (PSO) and DE in both robustness and speed [46]. SB-SADEA has also been demonstrated to aid in the accelerated design of very complex and highly-dimensional antennas, such as a metasurface-based lens antenna

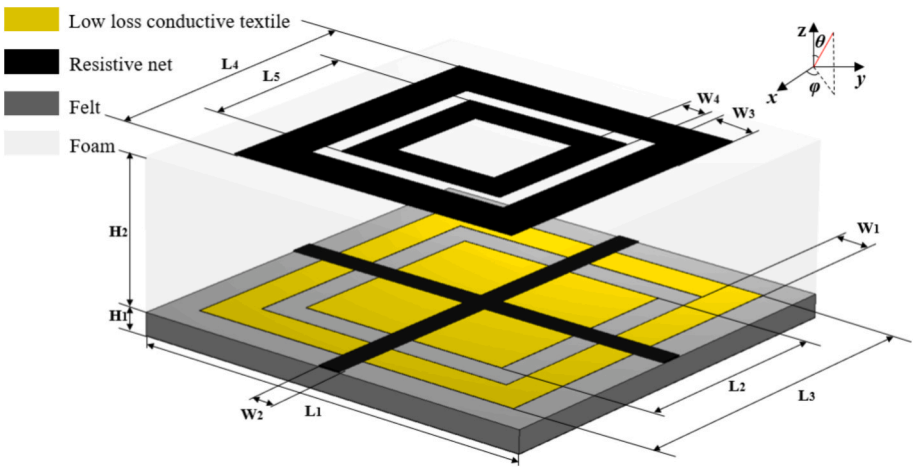

Fig. 1. The proposed design's unit cell shown schematically.

for millimeter-wave applications [47], making it an excellent choice for this work.

According to the simulation results, it can be observed that the proposed design can achieve in-phase reflection at 2.48 GHz and 5.84 GHz and absorb EM waves from 2.2 to 7.28 GHz with an angular stability of 30° and polarization-insensitivity when loaded with a lossy EBG layer. This work, to the best of the authors' understanding, introduces the first two-layer design capable of mechanical reconfiguration between reflection and absorption, relatively wide-band, polarization-insensitive, and angle-stable textile metasurface structure is being proposed. An equivalent circuit-based impedance matching approach is applied to the two-layer structure, with optimization carried out using the SB-SADEA method. The feasibility of the resulting design is verified through comprehensive full-wave simulations and experimental measurements.

The structure of the paper is as follows: Section 2 introduces the unit cell and the simulated performance of the MA. Section 3 analyzes the underlying absorption mechanism. Section 4 presents and discusses the experimental results, and Section 5 concludes the paper.

2. Design and analysis of simulation results

2.1. Structural design

The structural configuration and geometric parameters of the proposed unit cell are depicted in Fig. 1 ($L_1 = 38$ mm, $L_2 = 32$ mm, $L_3 = 20$ mm, $L_4 = 28$ mm, $L_5 = 16$ mm, $W_1 = 6$ mm, $W_2 = 8$ mm, $W_3 = 4.2$ mm, $W_4 = 3$ mm, $H_1 = 2$ mm, $H_2 = 13$ mm). The proposed absorbing EBG (AEBG) structure consists, from top to bottom, of a double-ring-shaped carbon-coated film with a square resistance of 200 Ω/sq, a foam substrate with a dielectric permittivity of 1.03 and a loss tangent (tan(δ)) of 0.0008, a crossed resistive network of carbon-coated film also uses 200 Ω/sq, a double-concentric square bandgap pattern made from conductive textile, a thin felt substrate characterized by a dielectric permittivity of 1.2 and loss tangent of 0.005, along with a plain conductive textile ground. The carbon-coated film and conductive textile, affixed onto the felt substrate, have an equal thickness of 100 μm. The ground makes the transmission zero through the structure, creating a barrier against undesired EM wave propagation. Simultaneously, a strategic application of the lossy EBG layer is employed, intricately loaded onto the reflective resonators. This approach aims not only to impede reflective surfaces but also to dynamically convert reflective EBG into absorptive EBG, enhancing the overall absorption characteristics. The structure exhibits functional reconfigurability: when the lossy EBG portion is eliminated from the design, its operational modality shifts completely to that of a reflecting EBG (REBG) implementation.

Table 2
Parameter ranges and SB-SADEA-based optimal design.

Item/parameters	Range	SB-SADEA optimum
L4 (mm)	24–36	25.72
L5 (mm)	8–24	16.54
W2 (mm)	1–5	4.87
W3 (mm)	1–8	2.51
W4 (mm)	1–8	1.91
H2 (mm)	1–15	15
P (s/m)	2–100	50
Q (s/m)	2–1000	50
Epsilon2 (units)	1–1.3	1.15
Bandwidth (GHz)	N/A	2.1–7.1
Time (h)	N/A	1.25 h

*The constraint for the value:$1\,\text{mm} < W4 < \frac{L5}{2}$, $L4 - 2 \times W3 - L5 > 1\,\text{mm}$. P denotes the conductivity of the top resistive film, while Q corresponds to that of the crossed resistive network.

The unit cell model is meshed in CST Studio Suite (CST) with a maximum of 10 tetrahedral elements per model box edge, resulting in approximately 15,000 tetrahedra. The analysis is performed using CST's frequency domain solver (FDS), which applies the finite element method (FEM). Boundary conditions include free space along the +Z and −Z directions, while periodic (unit cell) boundary conditions are imposed along the XY plane. The incident EM wave is set to be a plane wave parallel to the metasurface. The resistive sheets are simulated as low-conductivity surfaces in the design. The geometry of the unit cell model is then optimized using the SB-SADEA method to have its maximum in-band and minimum in-band return losses, within the frequency spectrum of 2.3–7.0 GHz, lower than −10 dB and −20 dB, respectively. The design parameters, their search ranges, and geometric constraints considered for the optimization are detailed in Table 2.

After 114 EM simulations (1.25 h), SB-SADEA achieved a unit cell with maximum in-band and minimum in-band return losses of −11.4 dB and −22.4 dB, respectively. The specifications of the proposed design are presented in Table 2, and its electromagnetic performance is subsequently evaluated through full-wave simulations conducted in CST, as discussed in the following subsections.

2.2. Simulation results of the ultra-light low-cost metamaterials

The simulated return loss for the unit cell operating in different modes (that is, AEBG, REBG, AEBG without crossed net, AEBG without REBG, and AEBG without REBG and ground) is presented in Fig. 2(a). Fig. 2(a) demonstrates that the proposed AEBG is capable of absorbing

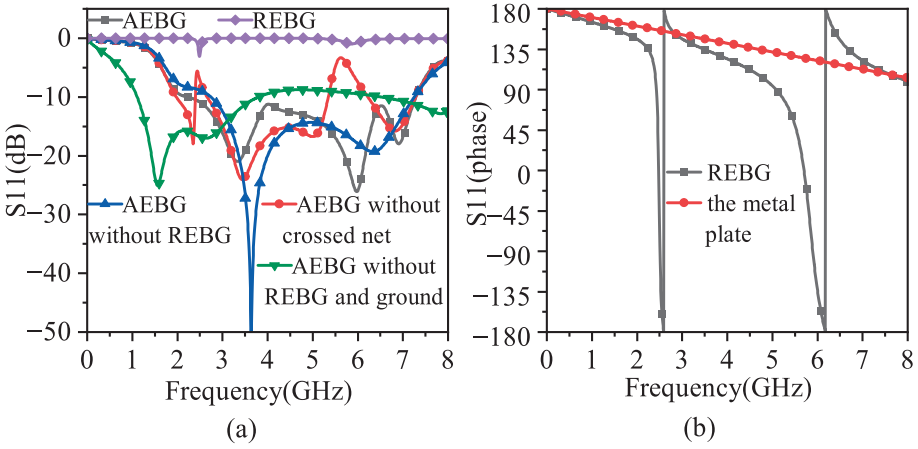

Fig. 2. (a) The reflection amplitudes in five cases. (b) The reflection phases in two cases.

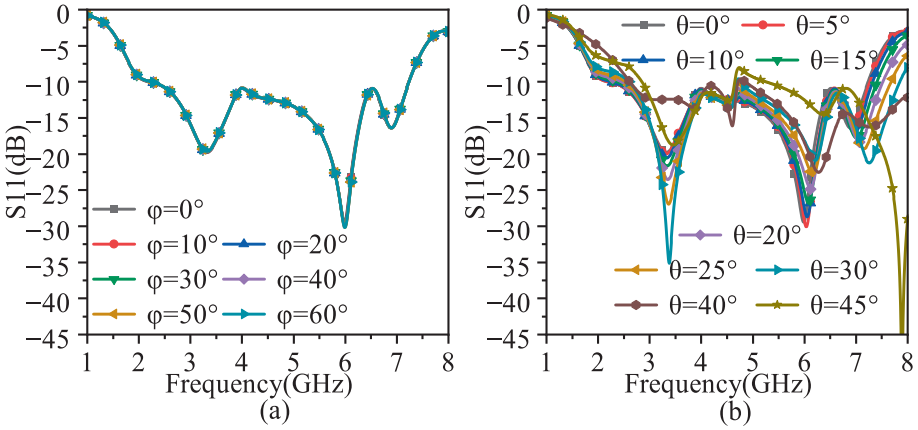

Fig. 3. (a) Absorption at different θ with $\varphi = 0°$. (b) Absorption at different φ with $\theta = 0°$ (Definition of theta and phi refer to Fig. 1).

nearly 90 % of incident electromagnetic energy within the 2.2–7.28 GHz frequency band. It is designed and realized for potential portable EM protection applications. Additionally, under the REBG configuration, the unit cell shows in-phase reflective responses at 2.48 GHz and 5.84 GHz, as shown in Fig. 2(b). It can be adapted to either a single-band antenna or a dual-band antenna. Also from Fig. 2(a), one can note that the absorption band of the AEBG mode is wider than AEBG without REBG mode, which proves that the bottom layer (REBG) not only functions as a reflector, but also broadens its absorption wideband, and the lossy EBG layer contributes to most of the energy absorption. The incorporation of the crossed resistive net assumes a pivotal role in reducing radar cross-section (RCS), specifically at the resonant frequencies (2.48 GHz and 5.84 GHz) associated with the reflective mode. The top double-ring-shaped resistive sheet is employed to tune the impedance, ensuring compliance with impedance matching principles. The lossy EBG layer serves as the primary region for energy dissipation, contributing significantly to the absorption of incident electromagnetic waves due to the substantial ohmic losses induced by current flow.

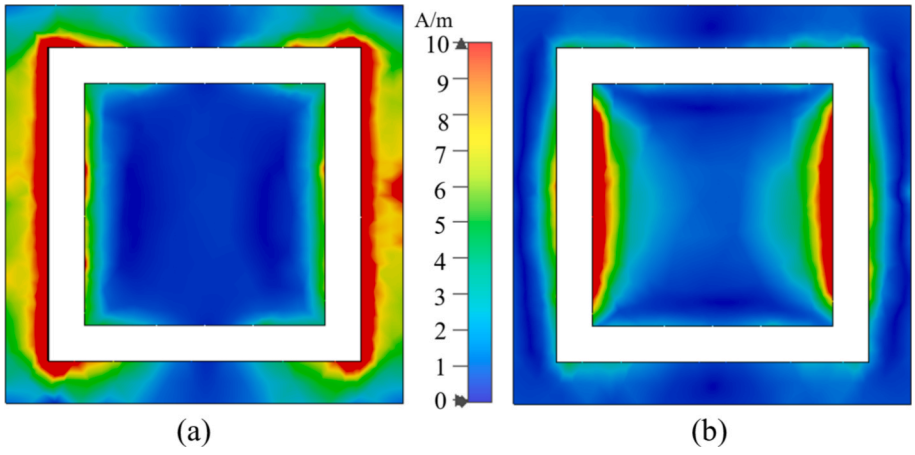

Fig. 4. (a) Distribution of surface currents on the REBG at 2.48 GHz. (b) Distribution of surface currents on the REBG at 5.84 GHz.

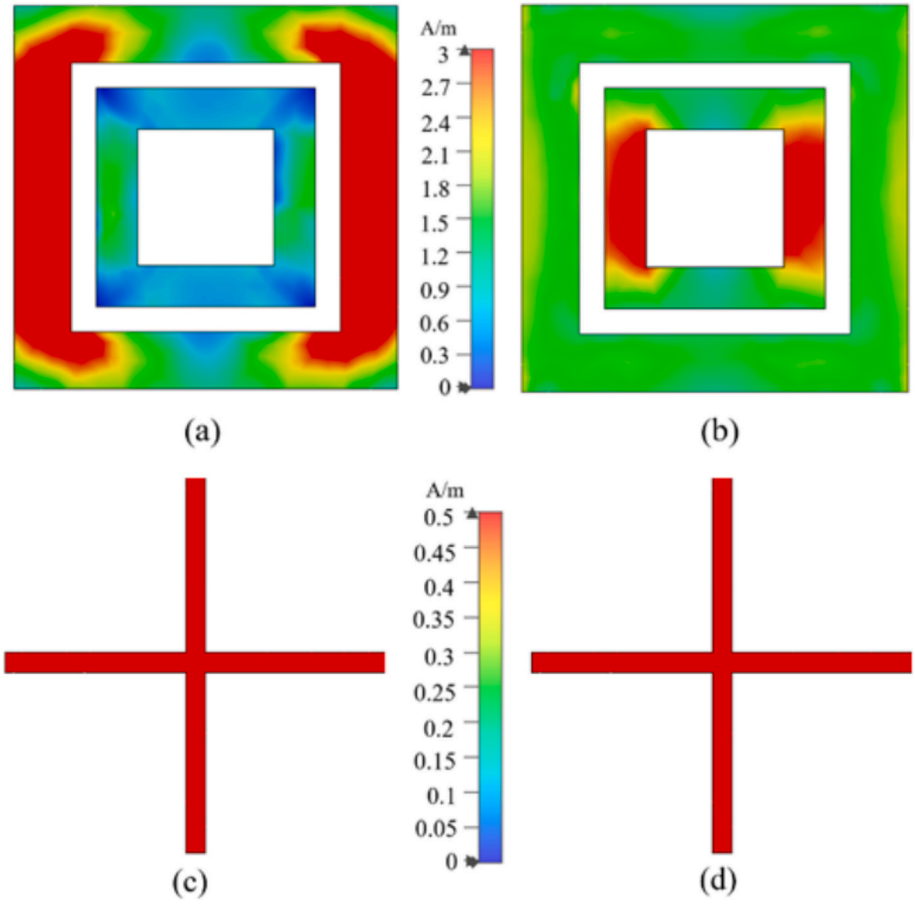

Fig. 5. Surface current patterns of (a) the double-ring-shaped resistive sheet at 2.48 GHz. (c) The crossed resistive net at 2.48 GHz. (b) The double-ring-shaped resistive sheet at 5.84 GHz. (d) The crossed resistive net at 5.84 GHz.

Together, these two layers function synergistically to realize an efficient absorber. Nevertheless, an additional peak emerges at 7 GHz due to the parasitic resonances originating from certain parts within the structure.

An investigation was conducted to evaluate how polarization angle and wave incidence angle affect the absorption properties. The angle θ corresponds to the inclination between the z-axis and the xz-plane, and the angle φ refers to the angle between the x-axis and the xy-plane. To evaluate polarization insensitivity, reflection amplitudes are calculated for multiple polarization angles (φ). Similarly, angular stability is examined by assessing reflection amplitudes at various incidence angles (θ). Fig. 3(a) shows the reflection amplitudes with different polarizations, by altering the angle from 0° to 60°. It is insensitive to different polarized electromagnetic waves. Fig. 3(b) depicts the variation in reflection amplitudes corresponding to incident angles ranging from 0° to 40°. It shows the relatively incident angle stability up to 40°. Stable absorption is achieved in all cases, confirming the metasurface absorber's dual advantages of wide-angle stability and polarization insensitivity.

3. Absorption mechanism

To clarify the underlying principle of the energy absorption for the proposed MA, the surface current, E-field, H-field distribution, and power loss density of the design at the resonant frequency are explored for EM waves with normal incidence. For the reflective mode, more currents are induced in the outer loop at 2.48 GHz, and the currents are concentrated in the inner patch at 5.84 GHz, as shown in Fig. 4(a) and (b). For the absorptive mode, the outer loop exhibits stronger induced currents at 2.48 GHz, while at 5.84 GHz, the currents are predominantly concentrated on the inner patch, as illustrated in Fig. 4(a) and (b). In the absorptive mode, the highest current densities appear along the edges of the resistive outer ring and the inner ring aligned with the incident electric field at 2.48 GHz and 5.84 GHz, respectively, as shown in Fig. 5 (a) and (b). Additionally, Fig. 5(c) and (d) demonstrate that the crossed resistive network also carries current, contributing to energy dissipation.

In addition, the power loss density and the distributions of the electric and magnetic field intensities at 2.48 GHz and 5.84 GHz were further simulated and analyzed, as illustrated in Fig. 6. As shown in Fig. 6(a), at 2.48 GHz, the electric field is primarily concentrated on both sides of the resistive square rings and within the dielectric substrate beneath the gap separating the rings. Fig. 6(b) indicates that at 5.84 GHz, the electric field is mainly localized at the edge of the inner ring and the adjacent substrate on its inner side. Meanwhile, the magnetic field distribution at 2.48 GHz is predominantly along the left and right edges of the outer ring, and at 5.84 GHz, it is concentrated on the corresponding sides of the inner ring, as presented in Fig. 6(c) and (d). Furthermore, Fig. 6(e) and (f) demonstrate that the power loss is chiefly focused on the sides of the square rings and the dielectric substrate below the gap between them.

The analysis can be further simplified with an equivalent circuit representation based on transmission-line theory, where the metasurface's unit cell is modeled as a network of impedance components [48,49]. According to Fig. 2(a), the S11 of AEBG has three resonance frequencies, and there are two resonance frequencies after removing REBG. So it can be inferred that the upper lossy EBG layer is analogous to two RLC parallel resonances, the whole AEBG is analogous to three RLC parallel resonances, and the substrate can be represented by an impedance Zo ($Zo = 377\ \Omega$), as shown in Fig. 7. The specific values stated as

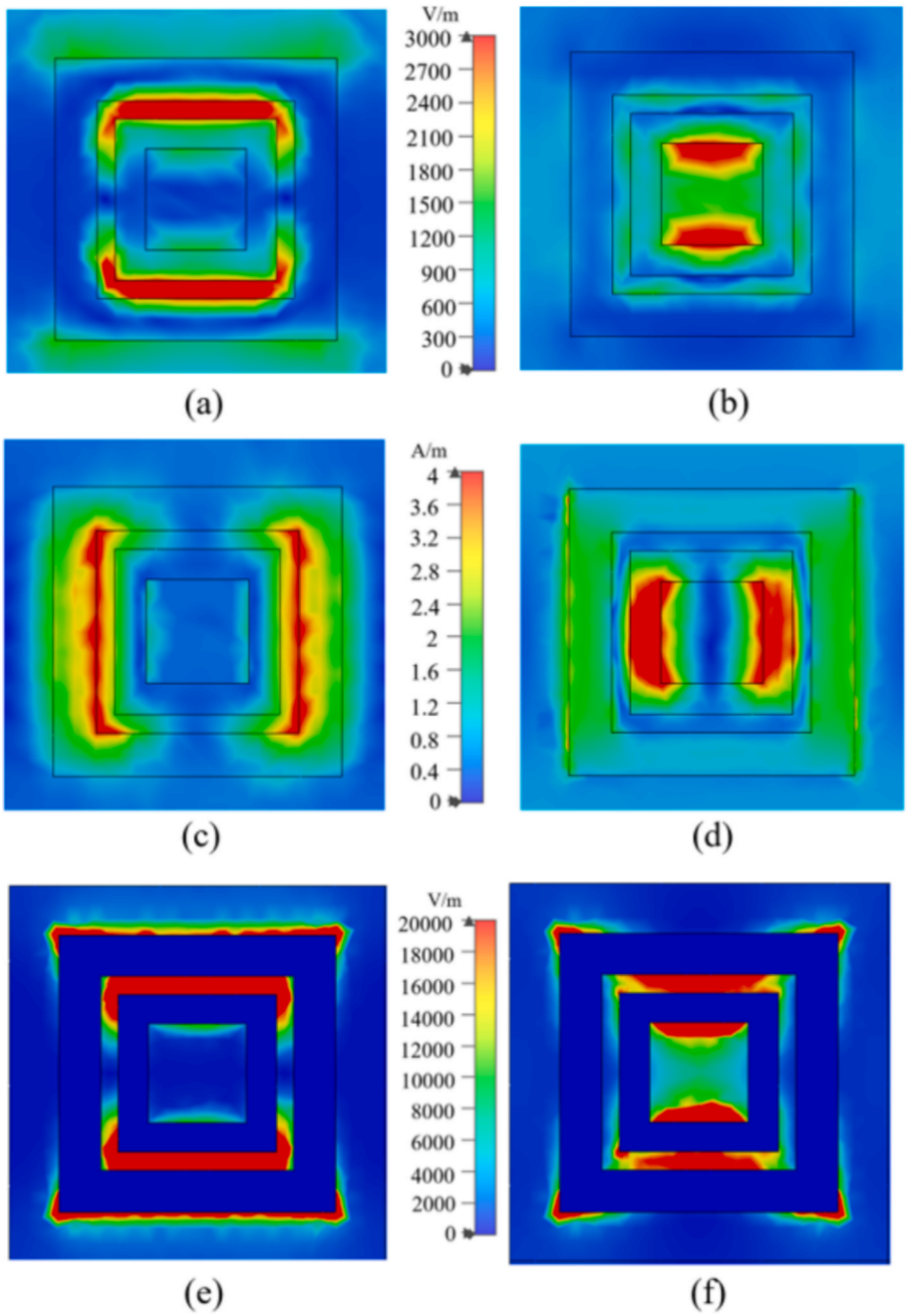

Fig. 6. Spatial distributions of the electric field, magnetic field, and power loss density of the designed metasurface absorber at (a, c, e) 2.48 GHz and (b, d, f) 5.84 GHz, respectively.

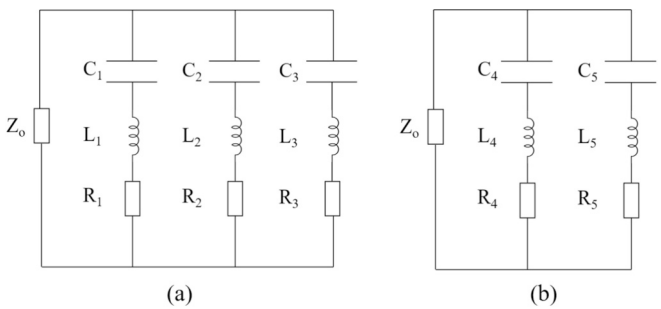

Fig. 7. The equivalent circuits of (a) AEBG, (b) AEBG without REBG or ground.

follows are obtained from the ADS simulations, $R_1 = 305\ \Omega$, $R_2 = 440\ \Omega$, $R_3 = 120\ \Omega$, $L_1 = 23$ nH, $L_2 = 46$ nH, $L_3 = 49$ nH, $C_1 = 0.124$ pF, $C_2 = 0.015$ pF, $C_3 = 0.009$ pF, $R_4 = 380\ \Omega$, $R_5 = 500\ \Omega$, $L_4 = 28$ nH, $L_5 = 35$ nH, $C_4 = 0.08$ pF, $C_5 = 0.016$ pF, exhibiting good correspondence with the simulation data, as shown in Fig. 8.

Fig. 9 presents the full-wave simulated absorptivity of the metasurface under varying foam thicknesses. It can be observed that as the foam thickness increases, the absorption first improves and then deteriorates, with the optimal performance achieved at around 13 mm. This trend indicates that there exists an optimal spacer thickness that ensures impedance matching between the metasurface and free space, thereby maximizing energy dissipation through the lossy layer. According to the transmission line theory, the input impedance Z_{in} of the metasurface structure depends on the foam thickness d as Eq. (1) [50]:

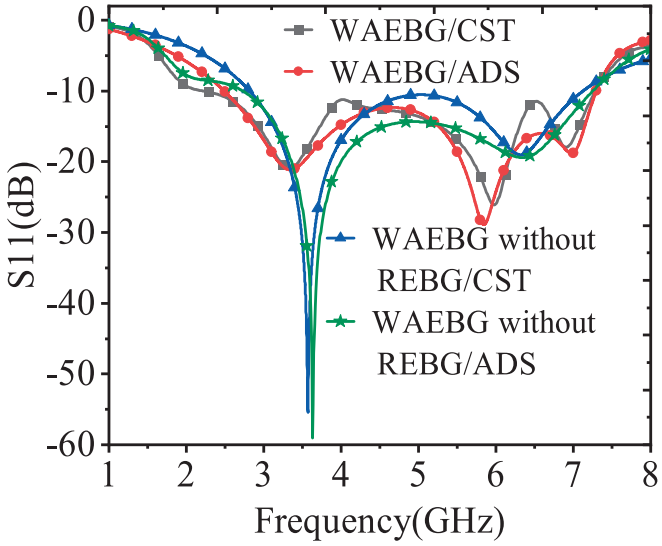

Fig. 8. Comparison of CST and ADS simulation results.

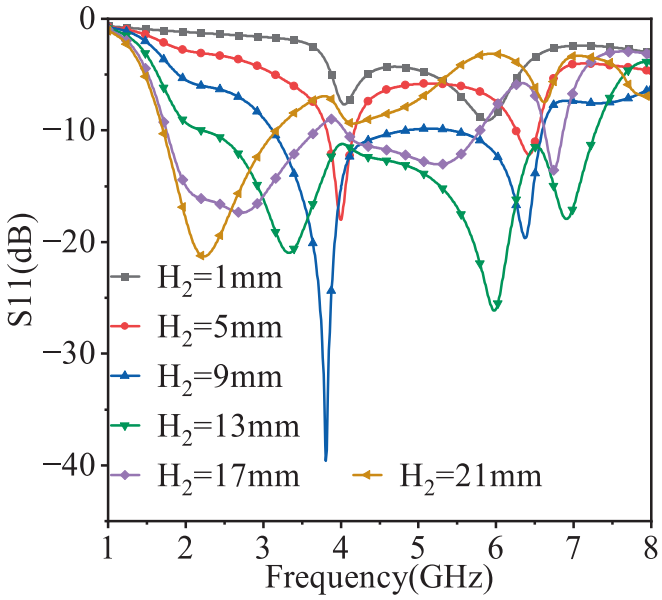

Fig. 9. The full-wave simulated absorptivity of the metasurface under varying foam thicknesses.

$$Z_{in} = Z_1 \cdot \frac{Z_{REBG} + jZ_1 tan(\beta d)}{Z_1 + jZ_{REBG} tan(\beta d)} \tag{1}$$

where Z_1 is the characteristic impedance of the foam layer, Z_{REBG} is the equivalent impedance of the REBG structure, and β is the phase constant in the foam. When Z_{in} approaches the free space impedance Z_0, the impedance matching is optimized, resulting in maximum absorption.

Fig. 10 demonstrates that the metasurface achieves excellent impedance matching with free space across the broadband frequency range of 2.2–7.28 GHz. This broadband absorption characteristic is achieved by introducing a lossy layer into the reactive electromagnetic bandgap (REBG) structure, which effectively modifies the impedance matching properties. As shown in Fig. 10, the normalized impedance exhibits real and imaginary parts approaching 1 and 0 respectively, as calculated by Eq. (2) [48,51,52], indicating optimal impedance matching conditions at the air-metasurface interface that enable broadband electromagnetic wave absorption.

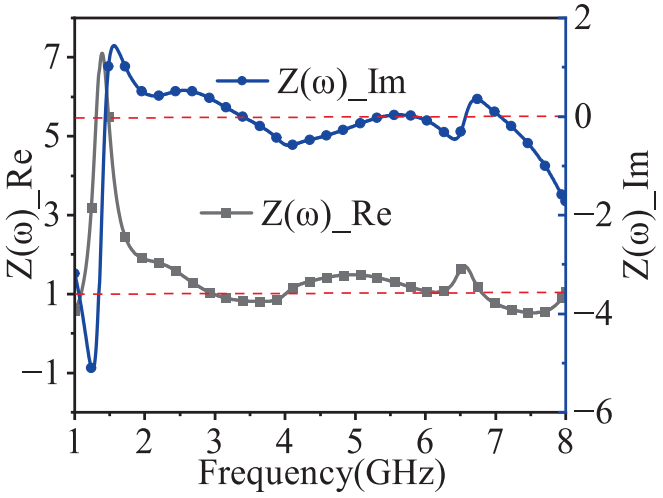

Fig. 10. Normalized input impedance of the metasurface in the absorbing state as a function of frequency at normal incidence.

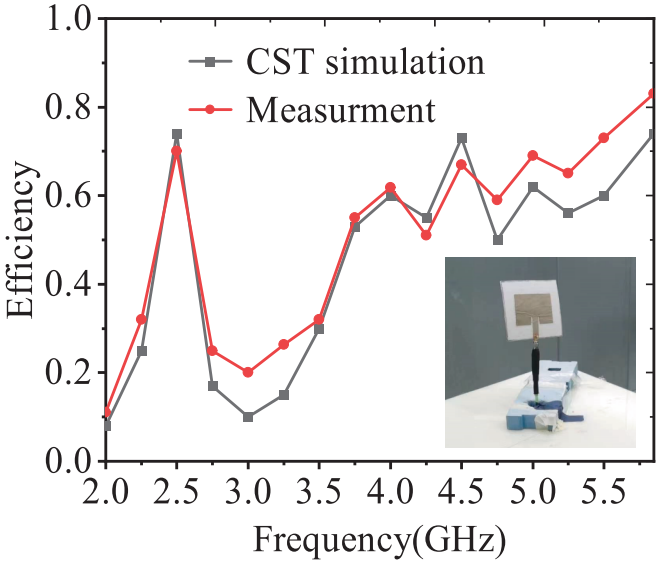

Fig. 11. The comparison of the patch antenna's efficiency.

$$Z(w) = \sqrt{\frac{(1+S_{11}(w))^2 - S_{21}^2(w)}{(1-S_{11}(w))^2 - S_{21}^2(w)}} = \frac{1+S_{11}(w)}{1-S_{11}(w)} \tag{2}$$

4. Experiment section

4.1. Material measurement

The composition of metasurfaces primarily involves conductive and dielectric materials. In this study, a conductive cloth woven with a plain weave structure from copper/nickel-coated polyester fibers is chosen as the conductive material, while a flexible and abrasion-resistant wool-blended felt (incorporating polyester fibers) is selected as the dielectric material. The key electromagnetic parameters of these two materials are then measured. The surface resistance of the conductive material affects its conductivity. In this work, the sheet resistance of the conductive material samples was evaluated utilizing the HPS2661 precision four-probe resistivity measurement system. This measurement method was employed to accurately determine the surface resistance, resulting in a measured sheet resistance of 23.8760 mΩ/sq. Additionally, the resistive

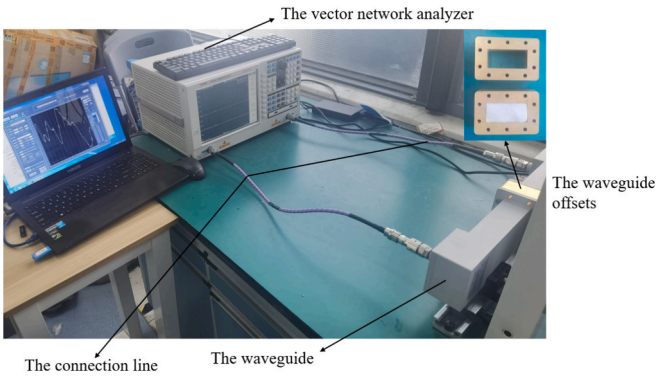

Fig. 12. The measurement setup for measuring the permittivity and dielectric loss tangent of the felt sample.

sheet resistance can be derived as follows Eq. (3):

$$R_S = \frac{1}{\delta \cdot t} \tag{3}$$

where δ is the conductivity of the prepared samples, and t is the thickness of the resistive sheet, which can be characterized by the thickness gauge.

To ensure consistency between the tested conductive fabric and simulated results, the efficiency of a textile patch antenna across the frequency range of 2–6 GHz is measured in an anechoic chamber to determine the textile's surface conductivity. The anechoic chamber, equipped with two reference standard gain horn antennas and a textile patch antenna. By comparing the measured efficiency data with CST simulation results using different conductivity settings (Fig. 11), the measured efficiency demonstrates strong agreement with the simulation results, thereby validating the appropriateness of this conductive textile as a material for textile-based metasurfaces.

The key parameters of dielectric materials are the dielectric constant and loss tangent. Therefore, the characteristics of the wool-blended felt are determined through the utilization of the waveguide transmission line method for measurement, which provides a comprehensive understanding of their behavior within the context of transmission line analysis. The measurement setup comprises a 3656BA vector network analyzer and two sets of waveguides as shown in Fig. 12. The measurement results are depicted in Fig. 13. From Fig. 13, these foam and felt materials exhibit relatively stable dielectric constants within the operating frequency range, with comparatively low loss tangents.

4.2. Fabrication of the ultra-light, low-cost metamaterial absorber

A fabricated metasurface prototype consisting of 12-by-12 unit cells was manufactured, and the image is depicted in Fig. 14. The single unit cell mass measurement using Shanghai Zhuojing Analytical Balance BSM120.4 is shown in Fig. 14(e), measured as 1.216 g. Calculations of mass per unit volume based on the densities of other common materials show that the proposed structure has a clear advantage in terms of weight. The substrate is made of felt material, while the patches and ground consist of a conductive textile with a surface conductivity greater than 10^5 S/m. The absorption properties of the fabricated prototype were assessed experimentally in an anechoic chamber, employing calibrated standard-gain horn antennas and an Agilent N5230C vector network analyzer. The measurement configuration is illustrated in Fig. 15. From a practical perspective, evaluating the bending and crumpling behavior of the proposed MA is essential. Therefore, the performance of the MA under bending and crumpling conditions was

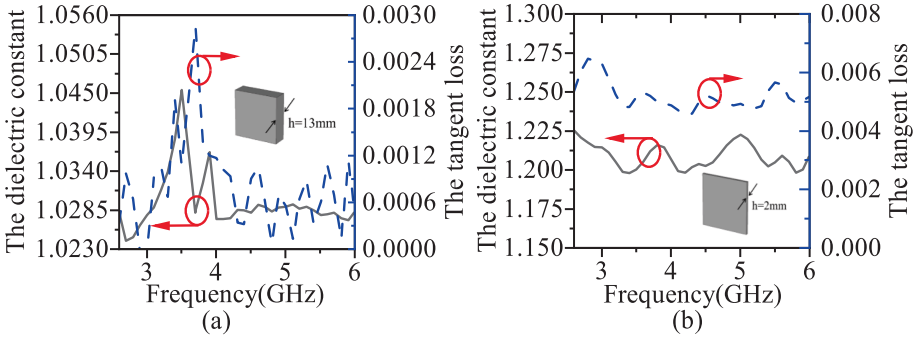

Fig. 13. The measured results of the foam and felt' dielectric constant and tangent loss at different frequencies. (a) Foam. (b) Felt.

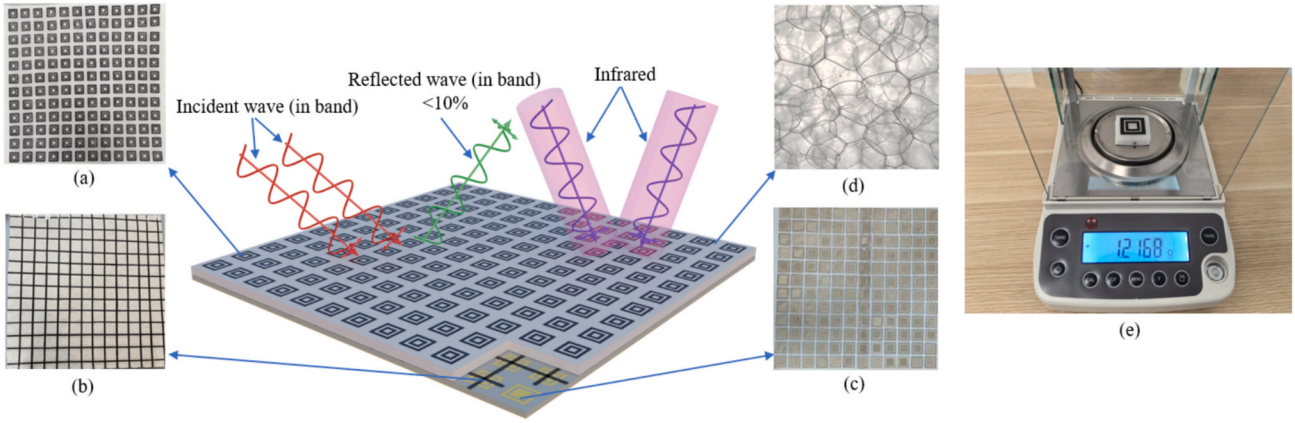

Fig. 14. The fabricated structure of (a) AEBG. (b) The crossed resistive net. (c) REBG. (d) The surface of the foam. (e) Measurement of unit cell mass using a high-precision balance.

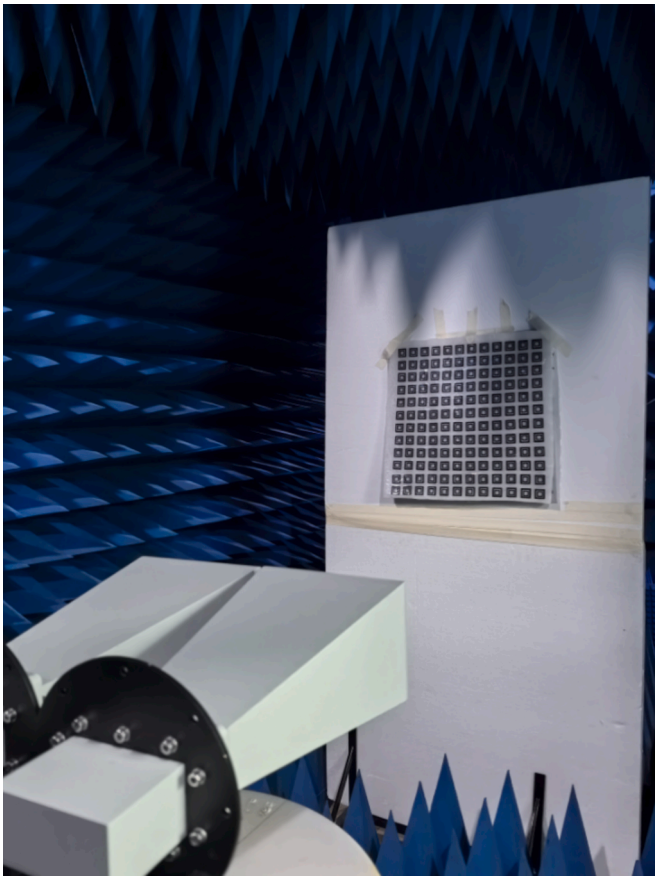

Fig. 15. The measurement setup for the absorption.

further investigated, with the corresponding results shown in Fig. 16. The results indicate that the proposed MA is flexible and deformation-insensitive. As shown in Fig. 17, the REBG improves the gain of monopole antennas at 2.48 GHz and 5.84 GHz by roughly 4 dB.

Fig. 18(a) and (b) show the testing environment for the super surface positioned with the front facing up and the back facing down on a preheating stage, respectively. The HIKMICRO K20 infrared thermal imager (a response band ranging from 7.5 to 14 μm) was used to test the infrared blocking effect of the super surface in both orientations. Fig. 19 indicates that at 80 °C, the side of the preheating stage with the super surface, whether the super surface is facing up or down, shows an infrared reading of approximately 28 °C on the thermal imager. This demonstrates that the structure exhibits infrared blocking capabilities, confirming that it possesses infrared isolation functionality. Additionally, based on the Stefan-Boltzmann law expressed in Eq. (4) [53]:

$$P = \varepsilon\sigma T^4 A \tag{4}$$

where P denotes the radiated power, ε represents the emissivity, σ is the Stefan–Boltzmann constant, T refers to the absolute temperature, and A is the surface area. The infrared emissivity can thus be determined based on the temperature-dependent radiation behavior, leading to Eq. (5):

$$E = \frac{T^4_{measured} - T^4_{ambient}}{T^4_{actual} - T^4_{ambient}} \tag{5}$$

where $T_{measured}$, $T_{ambient}$, and T_{actual} represent the temperature captured by the thermal imaging camera (28 °C), the surrounding ambient temperature (25 °C), and the actual surface temperature (80 °C), respectively. The calculation is performed by converting these values from Celsius to Kelvin, resulting in an estimated infrared emissivity of 0.06.

5. Conclusion

In conclusion, a low-cost, ultra-light dual-mode metasurface has been developed to perform either as an EBG-based reflector or a wideband absorber, depending on the presence of a lossy layer. Operating effectively within the 2.2–7.28 GHz range, the proposed design eliminates the need for manual parameter tuning by employing the SB-SADEA optimization algorithm to efficiently determine optimal geometric configurations. The underlying working mechanism has been thoroughly analyzed through surface current behavior, electromagnetic field distributions, power dissipation characteristics, and an equivalent circuit model. Fabrication and measurement of a prototype confirm the simulation results, validating both the electromagnetic and infrared camouflage performance. Furthermore, the design is scalable and can be extended to other frequency bands through appropriate geometrical adjustments, indicating its potential for broader applications in tunable and multifunctional electromagnetic devices. Compared to electronically reconfigurable metasurfaces, the proposed mechanical switching elimination complex circuit control and lowers fabrication cost. However, its response speed is slower due to manual installation or removal of the lossy layer, making it unsuitable for rapid or real-time applications. Future work could focus on semi-automated or responsive methods to improve switching speed.

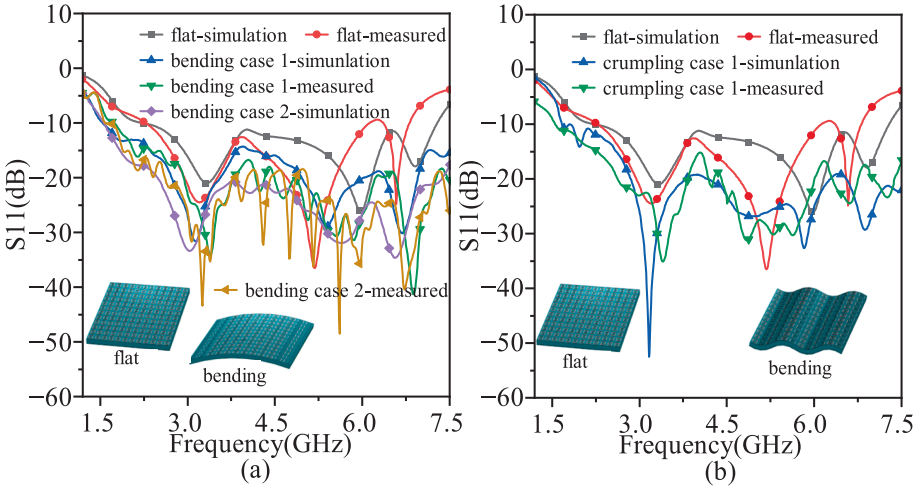

Fig. 16. Comparison between measured and simulated reflection amplitudes under varying curvature conditions: (a) flat versus bent states, and (b) flat versus crumpled states.

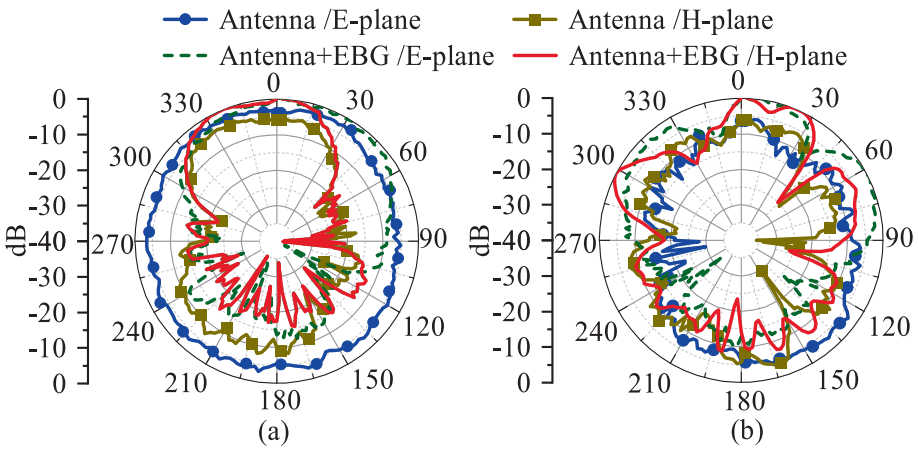

Fig. 17. Measured radiation pattern of a monopole antenna with/without the concentric squares REBG. (a) 2.48 GHz. (b) 5.84 GHz.

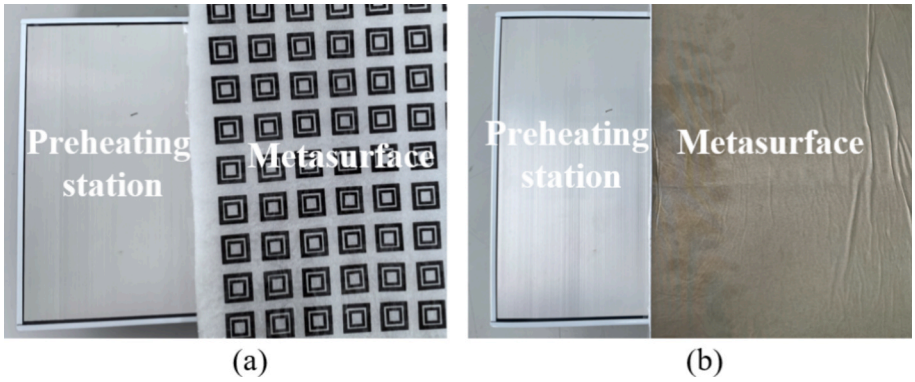

Fig. 18. Testing environment with the metasurface on the preheating station. (a) Metasurface facing upwards. (b) Metasurface facing downwards.

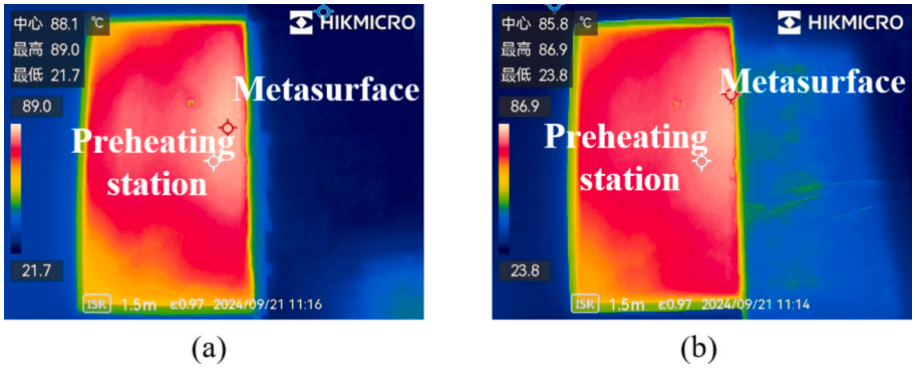

Fig. 19. Thermal infrared image of metasurface on a preheating station. (a) Metasurface facing upwards. (b) Metasurface facing downwards.

CRediT authorship contribution statement

Menglin Zhai: Writing – review & editing, Writing – original draft, Validation, Resources, Project administration, Methodology, Funding acquisition. **Tian Zhang:** Writing – review & editing, Writing – original draft, Validation, Methodology, Formal analysis, Data curation. **Rui Pei:** Visualization, Validation, Project administration, Funding acquisition, Conceptualization. **Huiwu He:** Writing – review & editing, Writing – original draft, Data curation. **Lei Zhang:** Visualization, Supervision, Funding acquisition. **Mark Leach:** Software, Resources, Investigation. **Eng Gee Lim:** Resources, Investigation. **Zhao Wang:** Resources, Investigation, Formal analysis. **Jingchen Wang:** Software, Resources, Data curation. **Qiang Hua:** Visualization, Validation, Software. **Mobayode Akinsolu:** Software. **Bo Liu:** Software, Resources. **Wen-Yan Yin:** Visualization, Validation, Supervision. **Yi Huang:** Visualization.

Funding

This work was supported by Zhejiang Key Laboratory of Intelligent Electromagnetic Control and Advanced Electronic Integration, the Natural Science Foundation of Shanghai under Grant 24ZR1403100, Shanghai Sailing Program under Grant 22YF1401000, and the National Natural Science Foundation of China under Grant 62371118.

Declaration of competing interest

The authors declare that they have no known competing financial interests or personal relationships that could have appeared to influence the work reported in this paper.

Acknowledgements

The authors would like to express their sincere gratitude to CST AG for providing access to the CST Studio Suite Electromagnetic Simulation Software through the China Key University Promotion Program. Appreciation is also extended to the Suzhou Municipal Key Laboratory for Wireless Broadband Access Technologies, Department of Electrical Engineering, Xi'an Jiaotong-Liverpool University (XJTLU), Suzhou, China, for offering essential research infrastructure. Support from the XJTLU Artificial Intelligence University Research Centre, the Jiangsu Province Engineering Research Centre of Data Science and Cognitive Computation at XJTLU, and the SIP AI Innovation Platform (YZCXPT2022103) is gratefully acknowledged. The authors also thank Nake New Materials for generously providing the carbon-coated resistive network materials used in this work.

Data availability

Data will be made available on request.

References

[1] K. Iwaszczuk, A.C. Strikwerda, K. Fan, X. Zhang, R.D. Averitt, P.U. Jepsen, Flexible metamaterial absorbers for stealth applications at terahertz frequencies, Opt. Express 20 (2012) 635–643, https://doi.org/10.1364/OE.20.000635.
[2] Y. Kato, S. Morita, H. Shiomi, A. Sanada, Ultrathin perfect absorbers for normal incident waves using dirac cone metasurfaces with critical external coupling, IEEE Microwave Wirel. Compon. Lett. 30 (2020) 383–386, https://doi.org/10.1109/LMWC.2020.2979708.
[3] B.-X. Wang, G. Duan, C. Xu, J. Jiang, W. Xu, F. Pi, Design of multiple-frequency-band terahertz metamaterial absorbers with adjustable absorption peaks using toothed resonator, Mater. Des. 225 (2023) 111586, https://doi.org/10.1016/j.matdes.2023.111586.
[4] Y. Yang, J. Wang, C. Song, R. Pei, J.M. Purushothama, Y. Zhang, Electromagnetic shielding using flexible embroidery metamaterial absorbers: design, analysis and experiments, Mater. Des. 222 (2022) 111079, https://doi.org/10.1016/j.matdes.2022.111079.
[5] R. Deng, K. Zhang, M. Li, L. Song, T. Zhang, Targeted design, analysis and experimental characterization of flexible microwave absorber for window application, Mater. Des. 162 (2019) 119–129, https://doi.org/10.1016/j.matdes.2018.11.038.
[6] I. V P, S. V P, V. C, S. Kumar T R, Design of broadband circuit analog absorber with optimal thickness for stable angular response in C, X, Ku, and K Bands, IEEE Trans. Electromagn. Compatibility 65 (2023) 2065–2069. doi: 10.1109/TEMC.2023.3298816.
[7] A. Bousselmi, A. Gharsallah, T.P. Vuong, Improving the gain of a multiband antenna by adding an AMC metasurface, in: 2023 Photonics & Electromagnetics Research Symposium (PIERS), 2023, pp. 2178–2183, https://doi.org/10.1109/PIERS59004.2023.10221384.
[8] X. Feng, X. Xie, M. Pu, X. Ma, Y. Guo, X. Li, X. Luo, Hierarchical metamaterials for laser-infrared-microwave compatible camouflage, Opt. Express 28 (2020) 9445, https://doi.org/10.1364/OE.388335.
[9] H. Li, H. Yuan, F. Costa, Q. Cao, W. Wu, A. Monorchio, Optically transparent water-based wideband switchable radar absorber/reflector with low infrared radiation characteristics, Opt. Express 29 (2021) 42863, https://doi.org/10.1364/OE.445942.
[10] H. Jing, Y. Wei, J. Kang, C. Song, H. Deng, J. Duan, Z. Qu, J. Wang, B. Zhang, An optically transparent flexible metasurface absorber with broadband radar absorption and low infrared emissivity, J. Phys. D Appl. Phys. 56 (2023) 115103, https://doi.org/10.1088/1361-6463/acbbda.
[11] M.M. Tirkey, N. Gupta, Broadband polarization-insensitive inkjet-printed conformal metamaterial absorber, IEEE Trans. Electromagn. Compat. 63 (2021) 1829–1836, https://doi.org/10.1109/TEMC.2021.3089830.
[12] Y. Fang, K. Pan, T. Leng, H.H. Ouslimani, K.S. Novoselov, Z. Hu, Controlling graphene sheet resistance for broadband printable and flexible artificial magnetic conductor-based microwave radar absorber applications, IEEE Trans. Antennas Propag. 69 (2021) 8503–8511, https://doi.org/10.1109/TAP.2021.3098538.
[13] D. Lee, H.K. Kim, S. Lim, Textile metamaterial absorber using screen printed chanel logo, Microw. Opt. Technol. Lett. 59 (2017) 1424–1427, https://doi.org/10.1002/mop.30558.
[14] Y. Yang, C. Song, R. Pei, J. Wang, Z. Liu, Y. Zhang, J. Shen, Design, characterization and fabrication of a flexible broadband metamaterial absorber based on textile, Addit. Manuf. 69 (2023) 103537, https://doi.org/10.1016/j.addma.2023.103537.
[15] Z.-J. Han, W. Song, X.-Q. Sheng, In-band RCS reduction and gain enhancement for a patch antenna array by using a 1-D periodic metasurface reflector, IEEE Trans. Antennas Propag. 67 (2019) 4269–4274, https://doi.org/10.1109/TAP.2019.2905989.
[16] A.J.A. Al-Gburi, I.B.M. Ibrahim, M.Y. Zeain, Z. Zakaria, Compact size and high gain of CPW-fed UWB strawberry artistic shaped printed monopole antennas using fss single layer reflector, IEEE Access 8 (2020) 92697–92707, https://doi.org/10.1109/ACCESS.2020.2995069.
[17] F. Wu, P. Hu, F. Hu, Z. Tian, J. Tang, P. Zhang, L. Pan, M.W. Barsoum, L. Cai, Z. Sun, Multifunctional MXene/C aerogels for enhanced microwave absorption and thermal insulation, Nano-Micro Lett. 15 (2023) 194, https://doi.org/10.1007/s40820-023-01158-7.
[18] C. Ma, M. Ma, C. Si, X. Ji, P. Wan, Flexible MXene-based composites for wearable devices, Adv. Funct. Mater. 31 (2021) 2009524, https://doi.org/10.1002/adfm.202009524.
[19] Z. Zhao, L. Zhang, H. Wu, Hydro/organo/ionogels: "controllable" electromagnetic wave absorbers, Adv. Mater. 34 (2022) 2205376, https://doi.org/10.1002/adma.202205376.
[20] D. Liu, Y. Zhang, C. Zhou, H. Lv, S. Chen, Y. Chen, S. Gao, B. Zhang, A facile strategy for the core-shell FeSiAl composites with high-efficiency electromagnetic wave absorption, J. Alloy. Compd. 818 (2020) 152861, https://doi.org/10.1016/j.jallcom.2019.152861.
[21] Y. Hou, Z. Sheng, C. Fu, J. Kong, X. Zhang, Hygroscopic holey graphene aerogel fibers enable highly efficient moisture capture, heat allocation and microwave absorption, Nat. Commun. 13 (2022) 1227, https://doi.org/10.1038/s41467-022-28906-4.
[22] S. Wang, Q. Liu, S. Li, F. Huang, H. Zhang, Joule-heating-driven synthesis of a honeycomb-like porous carbon nanofiber/high entropy alloy composite as an ultralightweight electromagnetic wave absorber, ACS Nano 18 (2024) 5040–5050, https://doi.org/10.1021/acsnano.3c11408.
[23] G. Deng, Y. Yang, Q. Zhou, Y. Lei, L. Yue, T. Yang, Lightweight and broadband electromagnetic wave absorbing foamed cement-based composites incorporated with hybrid dielectric fibers, Constr. Build. Mater. 327 (2022) 126931, https://doi.org/10.1016/j.conbuildmat.2022.126931.
[24] H. Tian, J. Lin, J. Liu, L. Li, B. Li, S. Zheng, W. Liu, C. Liu, Z. Zeng, N. Wu, Ultralight SiO_2 nanofiber-reinforced graphene aerogels for multifunctional electromagnetic wave absorber, ACS Appl. Mater. Interfaces 16 (2024) 61484–61494, https://doi.org/10.1021/acsami.4c16592.
[25] S. Zhu, R. Langley, Dual-band wearable textile antenna on an EBG substrate, IEEE Trans. Antennas Propag. 57 (2009) 926–935, https://doi.org/10.1109/TAP.2009.2014527.
[26] N.I. Landy, S. Sajuyigbe, J.J. Mock, D.R. Smith, W.J. Padilla, Perfect metamaterial absorber, Phys. Rev. Lett. 100 (2008) 207402, https://doi.org/10.1103/PhysRevLett.100.207402.
[27] S.-J. Li, X.-Y. Cao, J. Gao, T. Liu, Y.-J. Zheng, Z. Zhang, Analysis and design of three-layer perfect metamaterial-inspired absorber based on double split-serration-rings structure, IEEE Trans. Antennas Propag. 63 (2015) 5155–5160, https://doi.org/10.1109/TAP.2015.2475634.
[28] S. Sambhav, J. Ghosh, A.K. Singh, Ultra-wideband polarization insensitive thin absorber based on resistive concentric circular rings, IEEE Trans. Electromagn. Compat. 63 (2021) 1333–1340, https://doi.org/10.1109/TEMC.2021.3058583.
[29] Y.-Q. Li, H. Zhang, Y.-Q. Fu, N.-C. Yuan, RCS reduction of ridged waveguide slot antenna array using EBG radar absorbing material, IEEE Antennas Wirel. Propag. Lett. 7 (2008) 473–476, https://doi.org/10.1109/LAWP.2008.2001548.
[30] S. Tian, Y. Mu, Z. Li, X. Gao, H. Liu, L. Li, Transparent broadband wide-angle polarization-insensitive metasurface absorber for microwave antireflection, in: 2019 IEEE MTT-S International Wireless Symposium (IWS), 2019, pp. 1–3, https://doi.org/10.1109/IEEE-IWS.2019.8803967.
[31] X. Shen, T.J. Cui, J. Zhao, H.F. Ma, W.X. Jiang, H. Li, Polarization-independent wide-angle triple-band metamaterial absorber, Opt. Express 19 (2011) 9401, https://doi.org/10.1364/OE.19.009401.
[32] A. Zubair, M.Q. Mehmood, M. Zubair, Design of a fractal metasurface based terahertz broadband absorber, in: 2019 PhotonIcs & Electromagnetics Research Symposium – Spring (PIERS-Spring), 2019, pp. 663–666, https://doi.org/10.1109/PIERS-Spring46901.2019.9017639.
[33] B.-B. Xing, Z.-G. Liu, W.-B. Lu, H. Chen, Q.-D. Zhang, Wideband microwave absorber with dynamically tunable absorption based on graphene and random metasurface, IEEE Antennas Wirel. Propag. Lett. 18 (2019) 2602–2606, https://doi.org/10.1109/LAWP.2019.2944966.
[34] J. Tak, J. Choi, A wearable metamaterial microwave absorber, IEEE Antennas Wirel. Propag. Lett. 16 (2017) 784–787, https://doi.org/10.1109/LAWP.2016.2604257.
[35] O. Almirall, R. Fernández-García, I. Gil, Wearable metamaterial for electromagnetic radiation shielding, J. Textile Inst. 113 (2022) 1586–1594, https://doi.org/10.1080/00405000.2021.1940662.
[36] S. Ghosh, S. Lim, A multifunctional reconfigurable frequency-selective surface using liquid-metal alloy, IEEE Trans. Antennas Propag. 66 (2018) 4953–4957, https://doi.org/10.1109/TAP.2018.2851455.
[37] Y.J. Kim, J.S. Hwang, B.X. Khuyen, B.S. Tung, K.W. Kim, J.Y. Rhee, L.-Y. Chen, Y. Lee, Flexible ultrathin metamaterial absorber for wide frequency band, based on conductive fibers, Sci. Technol. Adv. Mater. 19 (2018) 711–717, https://doi.org/10.1080/14686996.2018.1527170.

[38] Y. Wu, J. Wang, S. Lai, X. Zhu, W. Gu, A transparent and flexible microwave absorber covering the whole WiFi waveband, AIP Adv. 9 (2019) 025309, https://doi.org/10.1063/1.5083102.
[39] P. Megh Sainadh, A. Sharma, S. Ghosh, Polarization-insensitive absorptive/transmissive reconfigurable frequency selective surface with embedded biasing, IEEE Antennas Wirel. Propag. Lett. 22 (2023) 164–168, https://doi.org/10.1109/LAWP.2022.3206098.
[40] T. Debogović, J. Bartolić, J. Perruisseau-Carrier, Dual-polarized partially reflective surface antenna with MEMS-based beamwidth reconfiguration, IEEE Trans. Antennas Propag. 62 (2014) 228–236, https://doi.org/10.1109/TAP.2013.2287013.
[41] W. Liu, P. Li, Z. Zhang, Q. Wang, W. Xu, Transmission-band-switchable absorptive/transmissive frequency selective surface using liquid metal, IEEE Antennas Wirel. Propag. Lett. 22 (2023) 144–148, https://doi.org/10.1109/LAWP.2022.3204784.
[42] H.L. Phan, D.T. Le, X.K. Bui, D.L. Vu, H.Q. Nguyen, N.H. Duong, T.M. Nguyen, T.Q. H. Nguyen, J.-M. Kim, High efficiency and ultra-wideband water-based microwave absorber using 3D printing, Opt. Commun. 556 (2024) 130297, https://doi.org/10.1016/j.optcom.2024.130297.
[43] T.Q.H. Nguyen, H.L. Phan, T.M. Nguyen, N.H. Nguyen, D.T. Le, X.K. Bui, D.L. Vu, J.-M. Kim, Switchable bi-functional water-based metasurface for high efficiency and wideband polarization conversion and absorption, Opt. Mater. 154 (2024) 115682, https://doi.org/10.1016/j.optmat.2024.115682.
[44] S.I. Sayed, K.R. Mahmoud, R.I. Mubarak, Design and optimization of broadband metamaterial absorber based on manganese for visible applications, Sci. Rep. 13 (2023) 11937, https://doi.org/10.1038/s41598-023-38263-x.
[45] M. Zhai, T. Zhang, R. Pei, M. Leach, E.G. Lim, Z. Wang, J. Wang, Q. Hua, M. Akinsolu, B. Liu, Y. Huang, A reflecting/absorbing dual-mode textile metasurface design, IEEE Antennas Wirel. Propag. Lett. 23 (2024) 3043–3047, https://doi.org/10.1109/LAWP.2024.3421549.
[46] Y. Liu, B. Liu, M. Ur-Rehman, M.A. Imran, M.O. Akinsolu, P. Excell, Q. Hua, An efficient method for antenna design based on a self-adaptive Bayesian neural network-assisted global optimization technique, IEEE Trans. Antennas Propag. 70 (2022) 11375–11388, https://doi.org/10.1109/TAP.2022.3211732.
[47] R. Mwang'amba, P. Mei, M.O. Akinsolu, B. Liu, S. Zhang, Gain bandwidth enhancement and sidelobe level stabilization of mm-wave lens antennas using AI-driven optimization, IEEE Antennas Wirel. Propag. Lett. (2024) 1–5, https://doi.org/10.1109/LAWP.2024.3382028.
[48] H.L. Phan, T.Q.H. Nguyen, J.-M. Kim, Multi-functional wideband metasurface: perfect absorber and linear to linear and linear to circular polarization converter, IEEE Access 12 (2024) 11664–11673, https://doi.org/10.1109/ACCESS.2024.3355135.
[49] D. Sievenpiper, R.F.J. Lijun Zhang, N.G. Broas, E.Y. Alexopolous, High-impedance electromagnetic surfaces with a forbidden frequency band, IEEE Trans. Microw. Theory Tech. 47 (1999) 2059–2074, https://doi.org/10.1109/22.798001.
[50] Q.-Y. Wen, Y.-S. Xie, H.-W. Zhang, Q.-H. Yang, Y.-X. Li, Y.-L. Liu, Transmission line model and fields analysis of metamaterial absorber in the terahertz band, Opt. Express 17 (2009) 20256, https://doi.org/10.1364/OE.17.020256.
[51] T.Q.H. Nguyen, H.L. Phan, V.D. Lam, J.-M. Kim, Design of an ultra-wideband and switchable VO_2 -based microwave absorber, Phys. Scr. 99 (2024) 075518, https://doi.org/10.1088/1402-4896/ad51af.
[52] D.T. Phan, T.K.T. Nguyen, N.H. Nguyen, D.T. Le, X.K. Bui, D.L. Vu, C.L. Truong, T. Q.H. Nguyen, Lightweight, ultra-wideband, and polarization-insensitive metamaterial absorber using a multilayer dielectric structure for C- and X-band applications, Physica Status Solidi (b). 258 (2021) 2100175, https://doi.org/10.1002/pssb.202100175.
[53] R. Karwa, in: Heat and Mass Transfer, Springer Singapore, Singapore, 2020, https://doi.org/10.1007/978-981-15-3988-6.